Synthesis, Characterization, Anti-Nematicidal, and Computational Study of Copper(II) Complex Derived From Fluoro-substituted Schiff Base Ligand

Salisu Y Lawan [1] , Naomi P Ndahi [1] , Ibrahim B Galadima [2] , Olaide O Wahab [3] , Tunde L Yusuf [4] , Louis-Charl C Coetzee [5] , Mostafa S Abd El-Maksoud [6] , Ibrahim Waziri [7,*]

[1] Department of Pure and Applied Chemistry, University of Maiduguri, Maiduguri, Nigeria.

[2] Department of Crop Protection, Faculty of Agriculture, University of Maiduguri, Maiduguri, Nigeria.

[3] Department of Chemical Sciences, University of Johannesburg, Doornfontein Campus, Johannesburg, South Africa.

[4] Department of Chemistry, Faculty of Natural Science and Agricultural Science, University of Pretoria, Pretoria, South Africa.

[5] Department of Chemistry, University of South Africa, Johannesburg, South Africa.

[6] Department of Pharmacology and Toxicology, Al-Azhar University, Assuit, Egypt.

[7] Department of Chemical Sciences, University of Johannesburg, Auckland Park Kingsway 2006, Johannesburg, South Africa.

***Correspondence**: Ibrahim Waziri (triumph2236@gmail.com)

Abstract

In this study, a novel fluoro-substituted Schiff base ligand (**HL**) was synthesized through a condensation reaction between 2-bromo-4-(trifluoromethoxy)aniline and 2-hydroxybenzaldehyde in methanol solvent at room temperature. The ligand was subsequently reacted with copper(II) acetate to produce the corresponding Cu(II) complex (**CuL_2**). Both the ligand and its complex underwent characterization using various techniques including nuclear magnetic resonance, ultraviolet-visible, Fourier-transform infrared, thermogravimetric analysis, elemental analysis, and mass spectroscopy. In addition, the solid-state structure of the complex was determined through single crystal X-ray diffraction analysis, confirming the successful isolation of the compounds. Subsequently, the nematicidal activities of the ligand and its complex were assessed through in vitro egg hatching inhibition and mortality rate assays, in comparison to the control, carbofuran (**Crf**), at concentrations of 50 and 100 µM over a 24–72-h period. The results indicated the ligand's superiority over the complex in both assays at lower concentrations. At a concentration of 50 µM, the ligand **HL** demonstrated 100% egg-hatching inhibition at 24, 48, and 72 h, whereas the complex **CuL_2** showed egg-hatching inhibition rates of 93.86 ± 0.22%, 98.76 ± 0.14%, and 99.33 ± 0.52% at the same time intervals. The control, **Crf**, exhibited inhibition rates of 56.33 ± 0.33%, 69.94 ± 0.6%, and 67.00 ± 0.34% over the same time period. Similarly, at a concentration of 100 µM, both the ligand and complex demonstrated 100% egg-hatching inhibition at 24, 48, and 72 h, while the control showed egg-hatching rates of 88.16 ± 0.84%, 89.9 ± 0.55%, and 90.8 ± 0.50%. Regarding the mortality rate, at 50 and 100 µM, the ligand **HL** exhibited a 100% mortality rate within 24 to 72 h, whereas the complex **CuL_2** displayed mortality rates of 56.66 ± 0.33%, 63.3 ± 0.23%, and 86.66 ± 0.13% at 24, 48, and 72 h, respectively, with a mortality rate of 100% at 100 µM within the same time intervals. The control, **Crf**, demonstrated mortality rates of 54%–67% at 50 µM and 62%–78% at 100 µM within 24–72 h. Additionally, the density-functional theory study revealed the electronic properties of the compounds, reinforcing the experimental findings.

1 Introduction

Nematode infestation poses a growing threat to agriculture globally, with developing nations particularly vulnerable to the devastating consequences of these parasitic worms on crop yields and food security [1-3]. Nematode resistance to conventional nematicides compromises the efficacy of control measures. This resistance intensifies the economic burden on farmers and stakeholders [4-6]. As nematodes develop resistance to these chemical treatments, the effectiveness of control strategies diminishes, leading to increased crop losses and reduced agricultural yields [7]. Currently, available nematocidal agents, including chemical compounds like carbamates and organophosphates, face challenges due to nematode resistance. For example, nematicides such as oxamyl (a carbamate) and ethoprophos (an organophosphate) have encountered reduced efficacy against nematodes like root-knot nematodes due to the development of resistance mechanisms. These instances highlight the pressing need for novel and sustainable solutions to effectively combat nematode resistance in agricultural settings. This phenomenon not only impacts the livelihoods of farmers but also contributes to food insecurity [2]. The challenges presented by nematode-induced diseases in crops are substantial due to the stealthy and evasive nature of these pests [8]. Furthermore, the diagnostic symptoms of nematode infestations closely resemble those of other pathogens and abiotic diseases, complicating accurate identification and control efforts [9-12]. Effectively addressing nematode infestations necessitates a clear comprehension of the issue at hand to explore enduring management strategies [13-15]. Currently, more than 783 million individuals worldwide are facing extreme hunger, with a staggering 2 billion people lacking adequate food security [16]. The second pivotal goal of the sustainable development goals (SDGs), established in New York in 2023, aims to end hunger, achieve food security, improve nutrition, and promote sustainability by the year 2030 [17, 18]. However, with approximately six years remaining until this target date, the enduring presence of plant-parasitic nematodes poses a significant threat to global food security, leading to the destruction of at least 12.3% of global food production annually, amounting to an estimated sum exceeding US$157 billion on a global scale each year [19]. Despite concerted efforts to address this pressing issue through various approaches and techniques, effective control mechanisms remain elusive. In response to this imperative, a cohort of researchers has shifted their focus toward identifying novel compounds that hold promise in combating nematode infestation [20, 21]. Various compounds were examined as potential nematocidal agents, encompassing both organic and metallo-based compounds. The metallo-based compounds specifically include those derived from Schiff bases. Schiff bases and their corresponding metal complexes present a wide range of biological properties, rendering them intriguing subjects for investigation as potential nematicidal agents [22-25]. Their adaptability in molecular design enables precise adjustment of their biological activities, particularly nematicidal properties. Numerous literature reports have showcased **Schiff base ligands** and their metal complexes that exhibit significant nematicidal activity against plant-parasitic nematodes. These compounds have demonstrated efficacy in addressing nematode infestations by interfering with crucial biological processes, underscoring their potential as eco-friendly alternatives to traditional nematicides [26-28]. El-Attar and co-researchers investigated the nematicidal activity of Co(II), Y(III), Zr(IV), and La(III) complexes derived from Schiff bases. Their research demonstrated the effectiveness of the synthesized complexes against second-stage juveniles under laboratory conditions, showing an inhibition rate of 100% [29]. Similarly, Meena and Fahim reported the nematicidal activity of vanadium(V) complexes derived from the Schiff base against Meloidogyne incognita, a nematode plant parasite. Their findings revealed that the complexes are more potent than the free ligand [30]. Also, Kavitha and Reddy reported the nematicidal activity of Ni(II) and Zn(II) complexes derived from **Schiff base ligands**, in which the complexes displayed higher activity than the free ligands [31]. Additionally, Kavitha et al. further reported Co(II) complexes derived from formyl chromone Schiff bases. These complexes were evaluated for their nematicidal activity on Meloidogyne incognita based on mortality rate and egg-hatching inhibition. The results obtained show that the ligands demonstrated superior activity than their corresponding complexes [32]. In another study, complexes of Cd(II), Mn(II), and Zn(II) derived from Schiff bases were evaluated for their nematicidal activity against Meloidogyne incognita, and the results show the complexes possess higher activity than the free ligands [28]. Among the Schiff base-derived nematocidal agents reported, only a few contain substituents known to enhance biological activity, such as fluorine, which improves binding to biological targets through conformational flexibility. In our current study, to boost nematicidal activity, we utilized a fluoro-substituted aldehyde to synthesize our Schiff base and then complexed it with Cu(II) ions to generate the corresponding complex. This choice was motivated by the demonstrated high affinity of fluorinated Schiff bases for interacting with biological membranes and disrupting cellular processes. Similarly, fluorinated Schiff bases have shown the capability to interact with DNA, a trait advantageous in the development of therapeutic agents [33-36]. Additionally, further complexation with copper, known for forming stable complexes with redox properties and high Lewis acidity, has the potential to enhance the biological efficacy and specificity of the compounds, thereby increasing nematicidal activity and broadening their applications in agricultural contexts [37-40].

2 Experimental

2.1 Materials and Instrumentations

All reagents were analytical grade (AR) and used without modification. Elemental analyses (CHN) were conducted using the VarioElementar III micro CHN analyzer. Infrared spectra were captured using both a Bruker Tensor 27 and a Perkin-Elmer Fourier-transform infrared (FTIR) spectrometer BX. The proton spectra were acquired on a Bruker 500 MHz spectrometer, whereas the carbon spectra were obtained using a Bruker 125 MHz spectrometer. Chemical shifts for the proton and carbon spectra were referenced to dimethyl sulfoxide (DMSO)-d_6 at chemical shifts of 2.50 and 39.50, ppm for proton and carbon, respectively, at room temperature. Electronic spectra were recorded at room temperature using a Shimadzu Ultraviolet (UV)-1900i Spectrophotometer, Double Beam. Mass spectra were generated via high-resolution mass spectrometry (HRMS) on a WatersAcquity Ultra-Performance Liquid Chromatography Synapt instrument at room temperature using high-performance liquid chromatography grade reagents. Thermo gravimetric analysis was carried out on an STDQ600 thermo analyzer with a heating rate of 10°C/min under a nitrogen atmosphere. Single crystal X-ray diffraction analysis was performed using a Bruker Apex DUO equipped with a 4K CCD diffractometer area detector system (positioned at a distance of 4 cm from the crystal), a graphite monochromator, and a Mo-Kα fine-focus sealed tube (λ = 0.71073 Å) operating at 1.35 kW power. The sample temperature was maintained at 173 (±2) K utilizing an Oxford 700+ series cryostream cooler.

2.2 Statistical Analysis

Using Statistix Version 9.0, every piece of data was subjected to analysis of variance in accordance with a completely randomized design. The least significant difference test at the 5% level of significance was used to evaluate the difference between the means.

2.3 Preparation of the Fluoro-Substituted Schiff Base Ligand

To synthesize this ligand, we employed a previously described literature procedure with slight modifications [41, 42]. A solution of 2-bromo-4-(trifluoromethoxy)aniline (1.70 g, 7 mmol, 1 eq) in 10 mL of methanol was added to a stirring solution of salicylaldehyde (0.8 g, 7 mmol, 1 eq) in 10 mL of methanol. Subsequently, three drops of formic acid (0.3 mL) were introduced to the mixture to aid the condensation process, which was then stirred at room temperature for 4 h, resulting in the formation of a yellow precipitate. The precipitate was separated via gravity filtration, washed with methanol to remove any unreacted chemicals, and dried to obtain a yellow solid, denoted as Schiff Base Ligand (**HL**). After drying, analytical and spectroscopic characterizations were carried out on the solid product to elucidate the structure of the ligand. The reaction pathway and details of condition for the reaction is shown in Scheme 1.

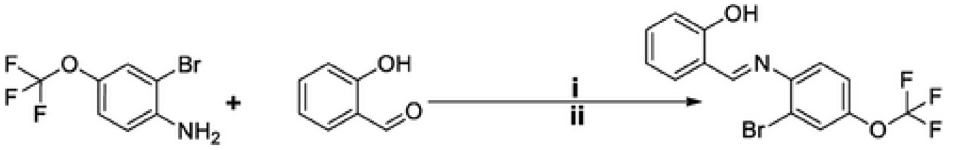

SCHEME 1. Synthesis of the fluoro-substituted Schiff base ligand; i = $CH_3OH/HCOOH$; ii = RT/ 4 h.

Yield: 88%; Color: Pale yellow; mp: 110°C; ^{1}H nuclear magnetic resonance (^{1}H NMR) (500 MHz, DMSO-d_6) δ(ppm): 12.74 (s, 1H, OH), 8.97 (s, 1H, HC=N), 7.85 (d, 1H J = 7.5 Hz, Ar-H), 7.69 (d, 2H, J = 8.5 Hz, Ar-H), 7.56-7.48 (m, 1H, J = 7.5 Hz, Ar-H), 7.46 (t, 1H, J = 8.5 Hz, Ar-H), 7.02 (t, 2H, J = 7.0 Hz, Ar-H); ^{13}C NMR (125 MHz, DMSO-d_6) δ(ppm): 165.4 (C=N), 160.2 (C-O, Ar-C), 146.4, 145.8, 134.1, 132.9, 125.6, 121.7, 121.1, 119.5, 119.3, 119.0, 116.7; UV-Visible (UV-Vis) (DMSO, 10^{-3} M) λ_{max} (nm): 270 ($\pi \to \pi^*$), 360 ($n \to \pi^*$); FTIR_{ATR} υ (cm^{-1}): 3200 (OH), 1618 (C=N), 1463 (C-N), 1355 (C-F), 1286 (C-O), 760 (C-Br); CHN Anal. Calculated for $C_{14}H_9BrF_3NO_2$; C, 46.69; H, 2.52; N, 3.89; found: C, 46.66; H, 2.51; N, 3.92; HRMS-ESI m/z $[M+H]^+$ = 361.9835 (Calculated for $C_{14}H_9BrF_3NO_2$, $[M+H]^+$ = 361.1339).

2.4 Preparation of the Copper(II) Complex

The complex was synthesized following a literature procedure with modifications [43]. Initially, the ligand **HL** (0.72 g, 2.0 mmol, 2 eq) was dissolved in 20 mL of dichloromethane in a reaction flask. Concurrently, a solution of $Cu(OAc)_2$ (0.18 g, 1.0 mmol, 1 eq) in 20 mL of methanol was slowly added while stirring. The resulting mixtures were stirred at room temperature for 4 h, leading to the formation of brown precipitates. These precipitates were subsequently filtered using gravity filtration, dried in a desiccator over fused calcium chloride, weighed, and the percentage yields calculated using a standard method. Subsequently, the complex underwent various characterization techniques. The reaction scheme and conditions are depicted in Scheme 2.

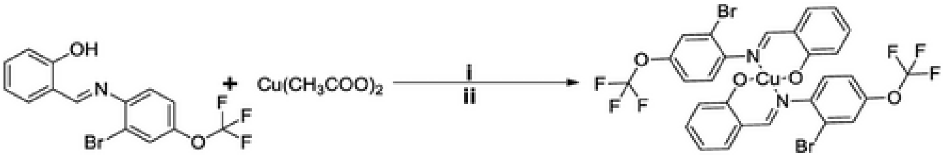

SCHEME 2. Synthesis of the complex (CuL_2); i = $CH_3OH/CHCl_2$; ii = RT/4 h.

Yield: 68%; Color: Brown; mp: 190°C; UV-Vis (DMSO, 10^{-3} M) λ_{max} (nm): 282 ($\pi \rightarrow \pi^*$), 387 ($n \rightarrow \pi^*$), 525 (d-d transition); $FTIR_{ATR}$ υ (cm^{-1}): 1600 (C=N), 1450 (C-N), 1440 (C-F), 1260 (C-O), 668 (C-Br), 554 (Cu-N), 434 (Cu-O); CHN Anal. Calculated for $C_{28}H_{16}Br_2CuF_6N_2O_4$; C, 43.02; H, 2.06; N, 3.58; Found: C, 43.02; H, 2.07; N, 3.57; HRMS-ESI *m/z* $[M+Na]^+$ = 803.554 (Calculated for $C_{28}H_{16}Br_2CuF_6N_2O_4$, $[M+Na]^+$ = 803.554).

2.5 Single-Crystal X-Ray Diffraction Analysis

The single crystal X-ray data for the Copper(II) complex (**CuL_2**) were collected using the APEXII software suite, with reflections indexed at various initial angles to devise a complete data collection strategy. Subsequently, the collected frames were integrated using the Bruker SAINT Software package for data processing [44]. SADABS was employed to mitigate absorption effects [45]. The structures were initially solved using the direct method with SHELXS and further refined with SHELXL [46]. Crystal structure graphics were generated using the Mercury software [47] Non-hydrogen atoms were analyzed isotropically and anisotropically based on F^2 using the full-matrix least squares method in SHELXL. Hydrogen atom positions were geometrically determined, allowed to ride on their parent atoms, and refined isotropically [48]. For methyl groups, initial C–H orientations were derived from the Fourier difference map and subsequently refined as rigid rotors.

2.6 Hirshfeld Surface Analysis

The calculation of Hirshfeld surfaces (HS) and two-dimensional fingerprint plots for the **CuL_2** complex was performed at the B3LYP/6-31G(d,p) level of theory using Crystal Explorer 17.5 software. CIF files were utilized as input files [49]. The generation of HS employed high-resolution and d-norm functions. Subsequently, the same software was employed to generate the 2D fingerprint plots.

2.7 Stability Study

The stability of the ligand and its complex was checked using repeated time-dependent analyses by UV-Vis absorption spectroscopy in a mixture of water and dimethyl sulfoxide in a 1:1 ratio at room temperature.

2.8 Nematicidal Activity Study

The synthesized ligand (**HL**) and its copper complex (**CuL_2**) were assessed for their nematicidal activity on *Melodogyne Incognita* through various assays, including egg hatching inhibition and mortality tests at concentrations of 50 and 100 μM, with each assay conducted in triplicate.

2.9 Isolation of the Nematode and Its Eggs

The nematodes were isolated using a method adapted from the literature [50]. Nematodes and their egg masses were extracted from severely affected okra roots by slicing the galls into smaller pieces and soaking them in water for 48 h. The decanted suspension was examined under a microscope to identify nematodes and their eggs; the presence of thread-like roundworms indicated the presence of nematodes. The stock suspension was stored in a refrigerator for subsequent nematicidal activity testing.

2.10 Egg-Hatching Inhibition

The egg-hatching inhibition was performed according to the literature [50]. The egg suspension was vigorously shaken for 5 minutes after the quick addition of 500 mL of 1% NaOCl. Subsequently, the suspension was swiftly poured through nested 500 and 200 mesh sieves. Eggs that passed through the 500 mesh sieves were retrieved through repeated sieving and rinsing, while those retained were washed with ample distilled water. The eluted eggs from the sieves were transferred to a beaker with water. The eggs retained on the sieve were thoroughly washed three times with distilled water and collected in a separate beaker. Approximately 10 nematode eggs were used per replicate sample, with each treatment replicated three times in the experiment conducted at room temperature. The eggs were treated with **CuL_2** and **HL** dissolved in concentrations of 50 and 100 µM/mL for 24, 48, and 72 h. Observations regarding egg hatching were recorded, and the percentage of egg hatching inhibition was calculated using the equation presented below,, where *n* = 10. The use of approximately 10 nematode eggs per replicate, replicated three times, strikes a balance between statistical rigor and practical feasibility in the experimental setup.

$$\%\text{Egg hatching inhib.} = \frac{\text{No. of nematodes in control} - \text{No. of nematodes in treatment}}{\text{No. of nematodes in control}} \times 100\%$$

2.11 Mortality Test

The ligand (**HL**), its complex (**CuL_2**), and the control, carbofuran (**Crf**), were initially dissolved in a mixture of methanol and distilled water to prepare dilutions of 50 and 100 µM/mL. The experiments were conducted under controlled laboratory conditions at room temperature. Approximately 10 freshly hatched second-stage juveniles were suspended in 5 mL of each diluted compound and then incubated. Distilled water containing nematode larvae served as the control. After incubation periods of 24, 48, and 72 h, deceased nematodes were observed under an inverted binocular microscope. Nematodes were deemed deceased if they displayed no movement when probed with a fine needle [32]. The percentages of mortality were calculated using Microsoft Excel software based on the equation shown below, and the resulting data were documented

$$\%\text{Mortality} = \frac{\text{Total no. of dead nematode juveniles}}{\text{Total no. of nematode juveniles (alive + dead)}} \times 100\%$$

2.12 Computational Studies

To account for the observed disparities in properties between Ligand (**HL**) and its copper(II) complex (**CuL$_2$**) from a quantum chemical point of view, input geometries of **HL** and **CuL$_2$** were neatly constructed in GaussView 5.0 interface [51] and optimized to their respective global equilibrium structures at B3LYP/ Def2TZVP theory level [52-55], using Gaussian 09 code, and ensuring that all necessary convergence and frequency conditions were satisfied (output geometries have no imaginary frequencies). The selected functional-basis set pair has remained one of the best choices for calculations involving ligand-metal systems [41, 56–59]. The relative reactivity of **HL** and **CuL$_2$** was assessed based on key reactivity descriptors derived from their respective highest occupied molecular orbital (HOMO) and lowest unoccupied molecular orbital (LUMO) energies, using Equations (1)–(4) [41, 60–63]. Relative susceptibility to nucleophilic and electrophilic attacks in biological systems was predicted based on electron density distributions of the optimized compounds as revealed by their electrostatic potential (ESP) map. Finally, the strength of the metal-ligand bonds in the complex was assessed based on natural bond orbital (NBO) analysis.

$$\text{HOMO - LUMO energy gap } (\mathrm{E_g}) = E_{LUMO} - E_{HOMO} \tag{1}$$

$$\text{Global softness (S)} = \frac{2}{\mathrm{E_g}} = \frac{2}{E_{LUMO} - E_{HOMO}} \tag{2}$$

$$\text{Chemical potential } (\Phi) = \frac{1}{2}(E_{LUMO} + E_{HOMO}) \tag{3}$$

$$\text{Electrophilicity index } (\omega) = \frac{\chi^2}{2\eta} = \frac{(-\Phi)^2}{\mathrm{E_g}} \tag{4}$$

3 Result and Discussion

3.1 Synthesis and Characterizations

The ON-donor bidentate fluoro-substituted **HL** was synthesized through the reaction of salicylaldehyde and 2-bromo-4-(trifluoromethoxy)aniline in methanol at room temperature, with formic acid serving as a catalyst. The mononuclear Cu(II) complex (**CuL$_2$**) was then obtained by combining Cu(OAc)$_2$ and the ligand in a 1:2 mole ratio in a dichloromethane/methanol mixture at room temperature. Both the ligand (**HL**) and the complex (**CuL$_2$**) were obtained in good yield and characterized using various analytical and spectroscopic techniques (ESI S1-S10). The structure of the complex (**CuL$_2$**) was further elucidated through single crystal X-ray analysis.

3.2 NMR Spectral Study

In the ^{1}H NMR spectrum of the ligand, **HL** (Figure S1), a distinctive chemical shift at 12.74 ppm was observed for the phenolic proton, while the azomethine proton was identified by a peak at 8.97 ppm. The downfield positioning of the signal due to the phenolic proton is attributed to the influence of the electronegative oxygen atom which withdraws electron density from the proton, leading to deshielding and appeared in the downfield region. In contrast, the signal due to azomethine proton was observed in the upfield region relative to the phenolic proton signal due conjugation, less shielding by the nitrogen atom and less acidic nature comparative to the hydroxyl group. The aromatic protons displayed chemical shifts ranging from 6.98 to 7.89 ppm, encompassing all the aromatic protons in the compound. The appearance of the signals due to the aromatic protons within this region is an indication of a complex interplay of electronic, ring current, structural, and solvent effects.

In the ^{13}C NMR spectrum of the ligand (Figure S2), distinct signals corresponding to all carbon atoms in the compound were observed. Notably, the azomethine (C═N) carbon exhibited a chemical shift at 165.5 ppm, while the carbon directly linked to the phenolic oxygen was identified at 160.2 ppm. The carbon atom due to the azomethine group was observed in downfield region at 165. 5 ppm due to the double bond character, electronegative nitrogen atom, and conjugation effect. But the aromatic carbon linked to the hydroxyl group was observed in the upfield relative to the azomethine carbon atom due to mesomeric effect of the hydroxyl group electron density. The remaining aromatic carbons were detected in the range of 116.7–146.4 ppm, collectively representing all the aromatic carbons in the compound. This signal fails within the expected range of aromatic carbons, which usually appears between 100 and 160 ppm. However, these signals were influenced by factors such as electron density, substitution pattern, and conjugation effects resulting in the observed range of 116.7–146.4 ppm.

However, due to the paramagnetic nature of the Cu(II) ion, NMR analysis could not be performed on the complex.

3.3 Electronic Spectral Study

The UV-Vis absorption spectral analysis of the ligand (**HL**) and its complex (**CuL$_2$**) was conducted in dimethyl sulfoxide using sample concentrations of 10^{-3} M, with the spectra presented in (Supplementary information Figure S4 and S8). Various absorption peaks were observed in the spectra. In the ligand's spectrum, two absorption peaks appeared in the UV region below 400 nm at 258 and 337 nm, corresponding to $\pi\rightarrow\pi^*$ and $n\rightarrow\pi^*$ transitions arising from the aromatic and azomethine moieties, respectively.

The complex's spectrum exhibited three absorption peaks at 284, 387, and 520 nm, attributed to $\pi\rightarrow\pi^*$, $n\rightarrow\pi^*$, and d-d transitions, respectively. A comparison of the ligand and complex spectra revealed differences: the peak at 258 nm in the ligand, associated with the $\pi\rightarrow\pi^*$ transition, shifted to 284 nm, while the absorption peak from the $n\rightarrow\pi^*$ transition at 337 nm in the ligand shifted to 387 nm in the complex. These shifts post-complexation could be ascribed to changes in ligand field strength and the involvement of the azomethine nitrogen in coordination.

Moreover, a new absorption peak was observed in the complex spectrum at 520 nm. The emergence of this peak in the visible region suggests that complexation with the Cu(II) ion introduced new electronic (d-d) transitions characteristic of the coordination environment and electronic structure of the complex.

The superimposed experimental and density-functional theory (DFT)-calculated spectra of the complex, **CuL$_2$** are presented in Figure 1. The DFT-calculated electronic spectrum of **CuL$_2$** agrees with the experimental spectrum with a correction value of 40 nm added to the wavelength. Both experimental and theoretical spectra displayed three absorption bands each from 270 to 520 nm. The visible band at 520 nm (1st excited electronic state) is decomposed into the following major contributions HOMO (α)→LUMO(α) (46%), H-4(β)→LUMO(β)

(31%), and HOMO(β)→L+1(β) (10%). The dominant contribution HOMO(α)→LUMO(α) in the visible region is due to d→d transition. The higher energy transitions at 387 nm major contributions were H-2(α)→LUMO(α) (12%), H-2(β)→L+1(β) (25%)→H-6(α)→L+1(α) (9%), H-4(α)→LUMO(α) (6%), and H-1(α)→L+8(α), while the 284 nm band major contributions were H-1(α)→L+1(α) (22%), HOMO(α)→LUMO(α) (12%)→H-12(α)→LUMO(α) (4%), H-11(α)→LUMO(α) (5%), H-4(α)→LUMO(α) (3%), and H-2(α)→LUMO(α). These high-energy LUMOs are metal-based and have mostly σ* character. Hence, the absorption at 284 nm is a π-σ* transition with significant ligand-to-metal charge transfer. The spectra presented in Figure 1 further corroborated that the experimental data agrees with the theoretic time-dependent-DFT data.

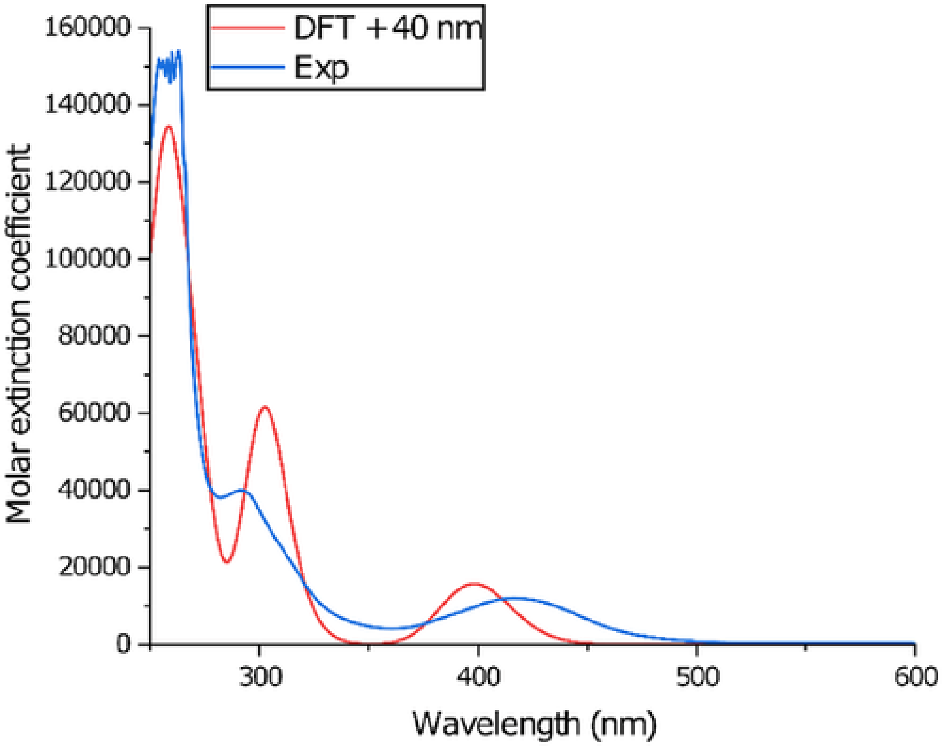

FIGURE 1. The experimental and density-functional theory (DFT) calculated spectra of CuL_2.

3.4 Infrared Spectral Analysis

The FTIR spectra of the ligand (**HL**) and its copper complex (**CuL_2**) were obtained in the solid state using the ATR method, and the spectra are presented in the Electronic Supplementary Information (Figures S3 and S7). The spectrum of the ligand (Figure S3) exhibits a phenolic O-H stretching frequency at 3200 cm^{-1}, an azomethine (C═N) transmittance peak at 1618 cm^{-1}, and stretching frequencies attributed to C─N and C─O at 1463 and 1286 cm^{-1}, respectively.

Upon comparing the spectra of the ligand and the complex after complexation, it was observed that the phenolic stretching frequency peak at 3200 cm^{-1} disappeared, indicating deprotonation and subsequent formation of a Cu─O bond stretching frequency, which was observed at 434 cm^{-1}. Similarly, the azomethine (C═N) stretching frequency at 1618 cm^{-1} in the free ligand shifted to 1600 cm^{-1} in the complex spectrum, suggesting the involvement of the nitrogen atom in complexation and the formation of a Cu-N bond with a stretching frequency at 554 cm^{-1}. The peaks associated with C-N and C-O underwent shifts to 1450 cm^{-1} and 1260 cm^{-1}, respectively, as a result of structural vibrations arising from complexation. The appearance of stretching vibration frequency due to Cu-O and Cu-N bonds justifies the formation of the complex.

3.5 Mass Spectral Analysis

To further confirm the formation of the ligand (**HL**) and its copper complex (**CuL$_2$**) and determine their stoichiometric composition, mass spectrometry analysis was conducted using HRMS. The spectra of **HL** and **CuL$_2$** are provided in the supplementary information (Figures S6 and S10), showing molecular ion peaks that correspond to the proposed structures of the compounds.

The spectrum of **HL** (Figure S6) reveals a peak with an m/z value of 361.9835, representing the molecular weight ionization with a proton $[M+H]^+$. This value closely matches the theoretically calculated value of 361.1339, confirming the successful isolation of **HL**. In the spectrum of the complex (CuL$_2$) (Figure S10), a molecular ion peak consistent with the proposed structure of the complex is observed, with an m/z value of 803.554 representing molecular ionization with sodium $[M+Na]^+$. This value coincides with the theoretically calculated value of 803.554 for $[M+Na]^+$. The agreement between the experimental and theoretical values provides confirmation of the formation of the complex.

Furthermore, the elemental (CHN) and metal (Cu) compositions of the ligand and its complex were quantified using microanalysis and metal analysis, and the result obtained support the proposed structures, confirming the 1:2 stoichiometric composition of **CuL$_2$** and the elemental composition of **HL**.

3.6 Thermogravimetric Analysis

The thermal decomposition of the compounds was investigated using thermogravimetric analysis under a nitrogen environment, with the corresponding thermograms depicted in Figures S5 and S9. The weight loss and decomposition temperatures were recorded within the range of 25–800°C.

The thermogram of **HL** (Figure S5) illustrates a single decomposition step occurring from 180 to 674°C, resulting in a weight loss of 63.41%, which was calculated as 65.20%. This decomposition phase represents the core organic fragment moiety of the ligand system. Additionally, the thermogram indicates the compound's stability within the range of 25–180°C, aligning with the compound's melting point (190°C).

Similarly, the thermogram of **CuL$_2$** (Figure S9) displays four distinct decomposition steps. The initial step, before 150°C, with a weight loss of 3.31%, is attributed to moisture content. The subsequent step, occurring between 190 and 230°C and resulting in a weight loss of 23.15% (calculated as 24.92%), corresponds to the organic fragment of the first ligand. The third decomposition step, observed at 250–350°C with a weight loss of 27.67% (calculated as 28.51%), is associated with the organic fragment of the second ligand. Finally, the fourth decomposition phase, spanning 380–700°C and leading to a weight loss of 11.44% (calculated as 11.93%), is linked to the inorganic residue within the molecule.

3.7 Description of Crystal Structure

The crystallographic analysis of the copper Schiff base complex, **CuL$_2$,** reveals that it crystallizes in the monoclinic space group *P21/c*. The asymmetric unit consists of a single molecular unit, where the copper ion is coordinated in a slightly distorted square planar geometry. The coordination environment includes two **HL**, each of which coordinates to the copper center through phenolic oxygen and an imine nitrogen atom. Figure 2 presents the structural representation of the **CuL$_2$** complex, highlighting this coordination arrangement.

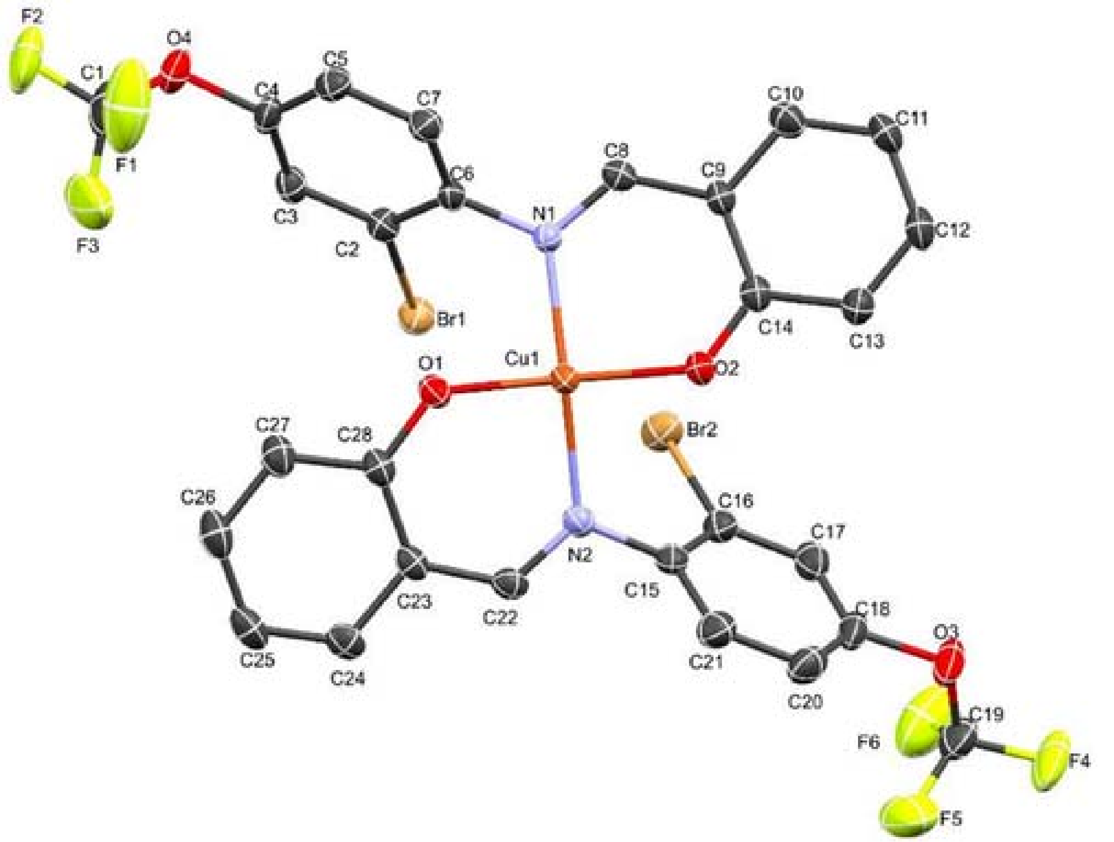

FIGURE 2. Labeled view of the low-temperature X-ray structure of CuL$_2$. Thermal ellipsoids are rendered at 50% for all complexes. Hydrogen atoms are omitted for clarity of the molecule.

Key crystallographic data and structure refinement parameters are presented in Table S1, providing essential information about the unit cell and crystal quality. Bond lengths and angles around the copper center, which are crucial for understanding its coordination geometry, are summarized in Table S2. The Cu1-O1 and Cu1-O2 bond lengths are measured at 1.889 and 1.883 Å, respectively, while the Cu1-N1 and Cu1-N2 bond lengths are 1.988 Å and 1.993 Å. These values indicate strong coordination between the copper ion and the donor atoms of the **HL**. Additionally, the C═N bond length is determined to be 1.429 Å, which is consistent with typical imine bonds and confirms the proper formation of the **HL** in the structure [64, 65]. The copper ion's coordination environment is based on square planar geometry, but slight distortions are observed due to steric and electronic effects from the **HL**. The bond angles around the copper center reflect these distortions: the O1-Cu1-O2 bond angle is 156.37°, deviating from the ideal 180°, and the N1-Cu1-N2 bond angle is 161.47°, showing a small contraction. Other bond angles, including N1-Cu1-O2 at 93.17°, N2-Cu1-O2 at 89.5°, N2-Cu1-

O1 at 93.12°, and O1-Cu1-N1 at 91.56°, are close to the ideal 90° but show minor deviations. These distortions are typical of copper(II) complexes, where factors such as ligand strain and electronic repulsion between donor atoms lead to slight deviations from perfect geometry.

The **HL**s' coordination through the phenolic oxygen and imine nitrogen atoms plays a key role in stabilizing the copper center. The observed bond lengths and angles are consistent with this coordination mode and provide insight into the structural dynamics of the complex.

Further analysis of the crystal structure revealed the presence of non-classical hydrogen bonding interactions within the lattice, which contributed to the overall stability of the structure. These unconventional hydrogen bonds, although weaker than traditional hydrogen bonds, still play an essential role in maintaining the integrity of crystal packing. In the C1 lattice, C2-Br1···O1 and C7-H7···C23 interactions occur between hydrogen atoms of the **HL** and neighboring **HL**. These weak interactions enhance the stability of the crystal structure and can influence the material's physical properties, including thermal stability and solubility. The crystallographic packing for C1, viewed along *b* axis is shown in Figure 3.

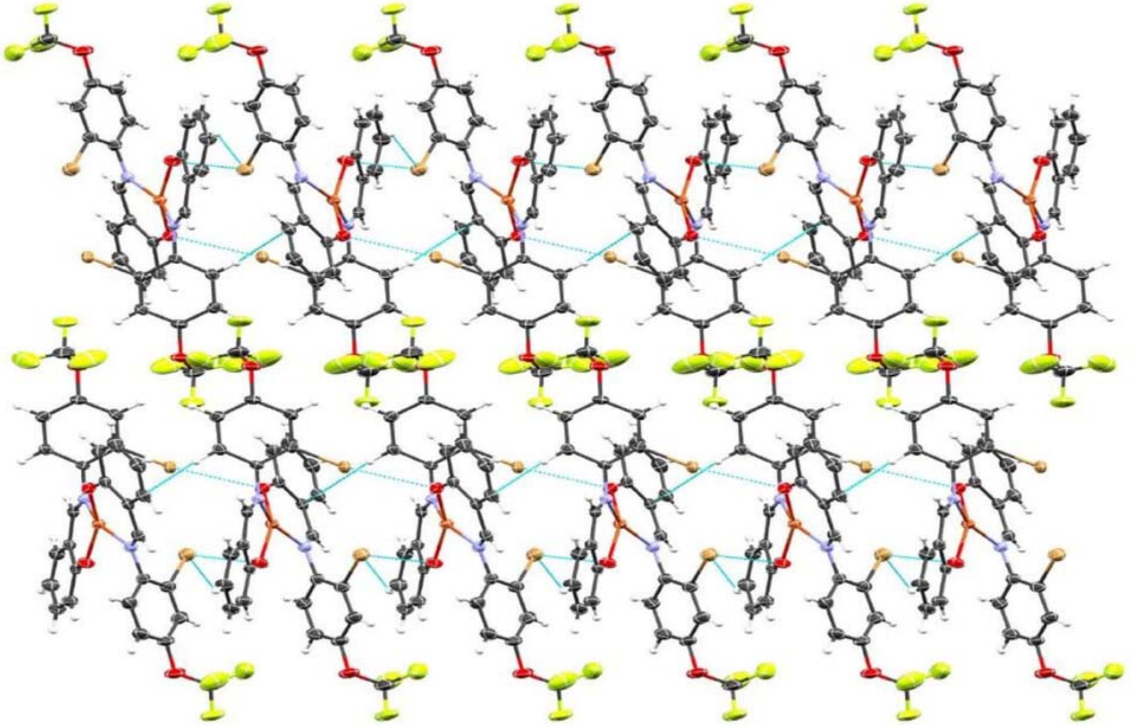

FIGURE 3. Crystallographic packing for CuL_2, viewed along the *b* axis.

3.8 Hirshfeld Surface

HS visually depicts the distribution of electron density surrounding molecules in crystals, highlighting areas of electron accumulation or depletion that play a key role in crucial intermolecular interactions like hydrogen bonding and van der Waals forces, essential for advancing knowledge in pharmaceuticals, materials science, and related fields. In this study, we only obtained the crystal structure of the complex, and it is confirmed to exist as $\mathbf{CuL_2}$, where two molecules of the ligand chelate the copper(II) ion. Therefore, to study the HS within the crystal lattice of **CuL_2**, the Crystal Explorer 17.5 software was employed to generate two-dimensional fingerprint plots by loading the CIF file of **CuL_2**. High-resolution analysis using the d_{norm} function was conducted, with a color scale ranging from red (0–0.701) to blue (1.798) a.u. [66]. The calculations involved two-dimensional fingerprint plots within the 0.6–2.6 Å range. An electron cloud was utilized to visualize interacting sites between neighboring molecules from the surface to the adjacent atom exterior (de plots) or interior (di plots) within the crystalline environment, with the normalized contact distance (d_{norm}) determined using Equation (1) [34, 67]. The results are displayed through colored isosurfaces, where bright red spots indicate strong interactions, white areas represent van der Waals interactions, and blue regions signify no interactions, as shown in Figure 4.

$$d_{norm} = \frac{d_{i-r_i^{vdw}}}{r_i^{vdw}} + \frac{d_{e-r_e^{vdw}}}{r_e^{vdw}} \qquad (1)$$

where r_i^{vdw} and r_e^{vdw} are the van der Waals radii of the atoms [39, 68, 69].

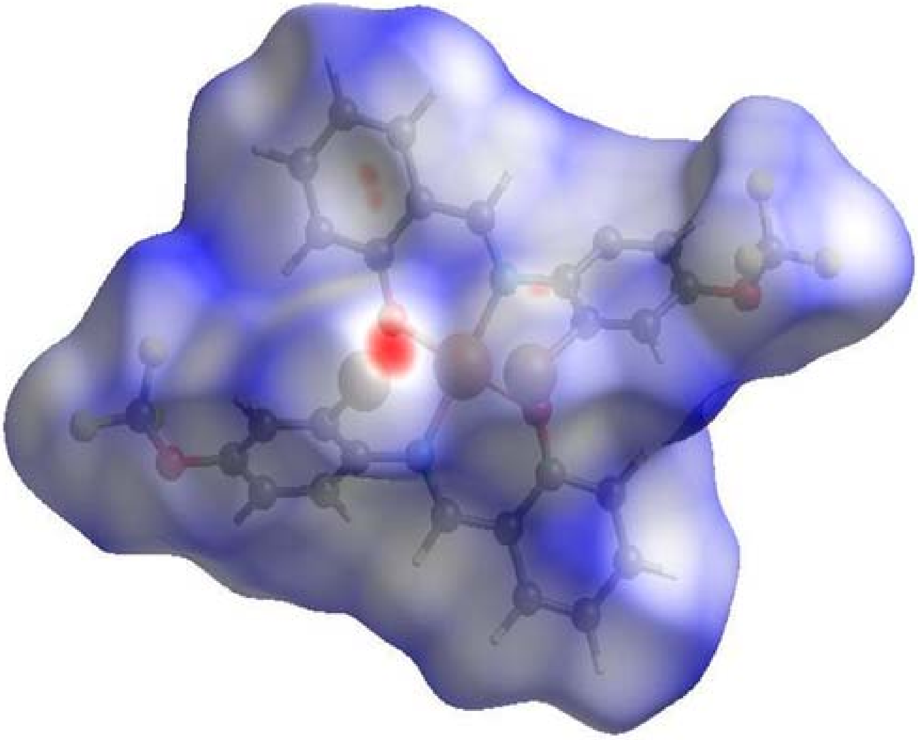

FIGURE 4. Hirshfeld surface analysis of CuL_2 obtained using Crystal Explorer 17.5 software with different color isosurfaces for the interacting sites in the crystalline environment.

Additionally, two-dimensional fingerprint plots of HS provide a quantitative value for the atomic contributions between interacting atoms within the crystalline environment (Figure 4). In this study, we noticed a significant number of contributions exceeded 1%. Among these atomic interactions, the dominance of interactions between hydrogen and fluorine atoms is evident, with contributions exceeding 15%. This is likely attributed to hydrogen bonding. Additionally, strong interactions such as C-H/H-C and H-H interactions exhibit contributions exceeding 10%, consistent with observations from our previous studies [34, 39].

Furthermore, notable interactions between bromine and fluorine atoms were observed, with contributions close to 5%. These interactions are also likely influenced by hydrogen bonding. The details of all the interactions within the 2D fingerprint plot are shown in the supplementary information (Figure S11).

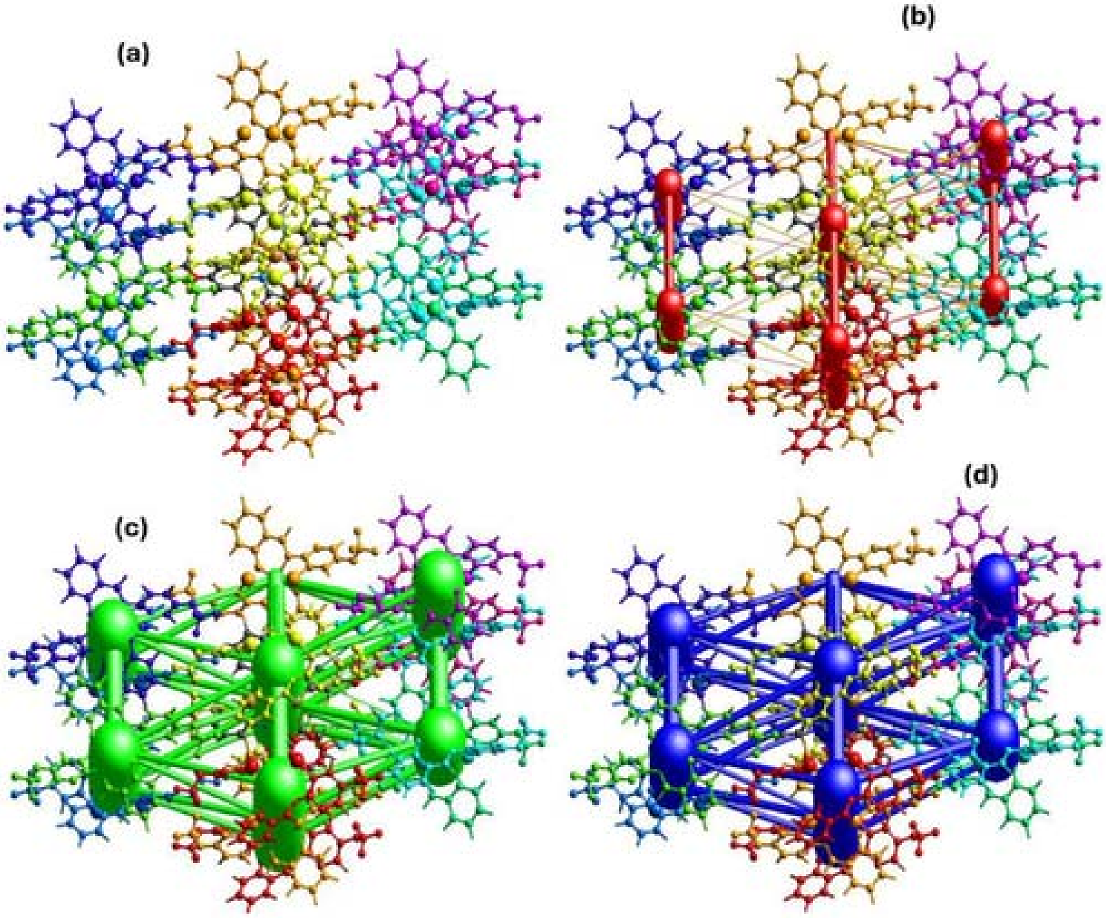

FIGURE 5. The intermolecular interaction between the neighboring molecules (a), Coloumbic interacting topology between interacting atoms on neighboring molecules (b), Dispersion interacting topology network between interacting atoms on the neighboring molecules (c), and Total interacting topology network between interacting atoms on the neighboring molecules (d) within the crystalline environment of CuL_2 generated on Crystal Explorer 17.5 software using the Tonto method at the B3LYP/DGDZVP level of theory.

The intermolecular interacting energies between the neighboring molecules within the crystalline environment were estimated using the Tonto method at the B3LYP/DGDZVP level of theory [70]. These energies were visualized using color schemes, where the same color signifies interacting energies between these adjacent molecules as depicted in (Figure 5a). Furthermore, the intermolecular topology framework was established by connecting the interacting atoms of these neighboring molecules, highlighting what is known as Coulombic interactions as shown in (Figure 5b). The Coulombic interactions reveal the distribution of charge density around the metal center and ligands. These interactions provide insights into the electrostatic forces at play within the complex and reinforce the bonding patterns, intermolecular interactions, and the overall stability of the **CuL_2** in its crystalline environment. The notable among is Br-Cu interaction which accounts for 6% of the overall interactions and enables us to obtain a dispersion interaction between the atoms of neighboring molecules (Figure 5c), which reveals non-covalent interactions between metal ions and ligands in the crystalline environment and Total interactions therein (Figure 5d). The total interactions gave deeper insight into the complex interplay between different types of interactions within the crystal environment, offering a more thorough understanding of the structural and chemical characteristics of the **CuL_2** complex.

Quantitative values for these interactions resulting from symmetry operations (Sym op) were determined, with R representing the distance between the molecular centroids of the interacting molecules (Table S3), derived from vector properties [71]. The interaction between neighboring molecules induces a perturbation, leading to an energy breakdown as shown in Equation 2:

$$E_{tot} = E_{ele} + E_{pol} + E_{dis} + E_{rep} \tag{2}$$

Here, E_{ele}, E_{pol}, E_{dis}, and E_{rep} represent electrostatic, polarization, dispersion, and repulsive energies, respectively [72]. Consistent with our previous studies [43], a correlation between R and E_{tot} was observed, with a few outliers where stronger interaction energies occur at shorter intermolecular centroids.

Overall, the Hirshfeld analysis of the complexes emphasized a significant interaction within the crystal environment of the compound, revealing its crystal stability and potential as a biologically viable molecule. Additionally, this study showcased the compound's inclination to interact favorably with receptors, resulting in a favorable binding score. This result corroborated the results of the Hirshfeld analysis conducted on some biologically viable metal complexes [73-75].

3.9 Biological Study

3.9.1 Stability Study

The stability of a meta-based biological agent at an early investigational stage is crucial for several reasons, including its ability to endure in an aqueous environment. Many metallodrug candidates, such as auranofin (Au(I)), cisplatin (Pt(II)), and NAMI-A (Ru(II)), undergo ligand exchange reactions, ultimately transforming into simpler (ionic) metal species both in vitro and in vivo [76, 77]. Therefore, before subjecting the synthesized Cu(II) complex **CuL_2** to the biological study, it was assessed for stability in a phosphate buffer (10% (v/v) DMSO) over a period of 72 h using UV-visible spectroscopy (Figure S12). Spectral changes indicated that **CuL_2** remained relatively stable over a 72-h period in the phosphate buffer (Figure S12). No observable chemical alterations, such as metal ion release or bond dissociation, occurred during this timeframe. The absence of isosbestic points in the spectrum suggests that **CuL_2** did not undergo any chemical reactions within the investigated period. Therefore, this suggests the compound will make a suitable investigational biological candidate to test further.

3.9.2 Anti-Nematocidal Activity Study

After conducting a stability study on the **CuL_2** complex (Figure S12), which indicated its stability in an aqueous medium, **CuL_2** was evaluated for its anti-nematocidal activities on nematodes using *Melodogyne Incognita* (second-stage juveniles (J2)) and their eggs using in vitro egg hatching inhibition and mortality rate assays. This evaluation involved comparisons with the ligand **HL** and the control **Crf**. The assays were performed using concentrations of 50 and 100 µM over a 24–72-h period (Figures 6 and 7). The results revealed that both the ligand and the complex exhibited superior activity compared to the control at both concentrations. Interestingly, the ligand (**HL**) demonstrated greater activity than the complex (**CuL$_2$**) at lower concentrations.

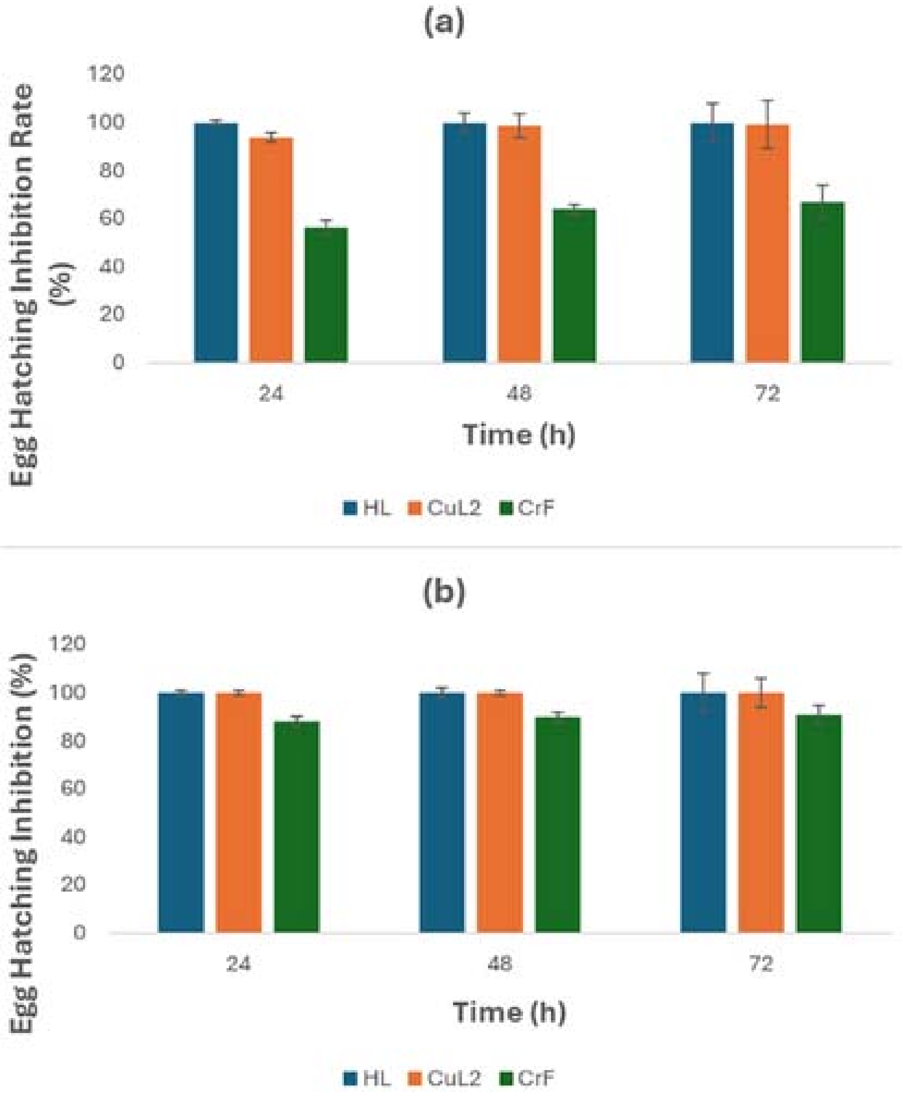

FIGURE 6. Plot of the egg hatching inhibition activity of the ligand (HL), and its copper complex (CuL$_2$), comparative to control, carbofuran (Crf) as a function of time after 24, 48, and 72 h; after treatment with samples concentrations of (a) 50 µM and (b) 100 µM.

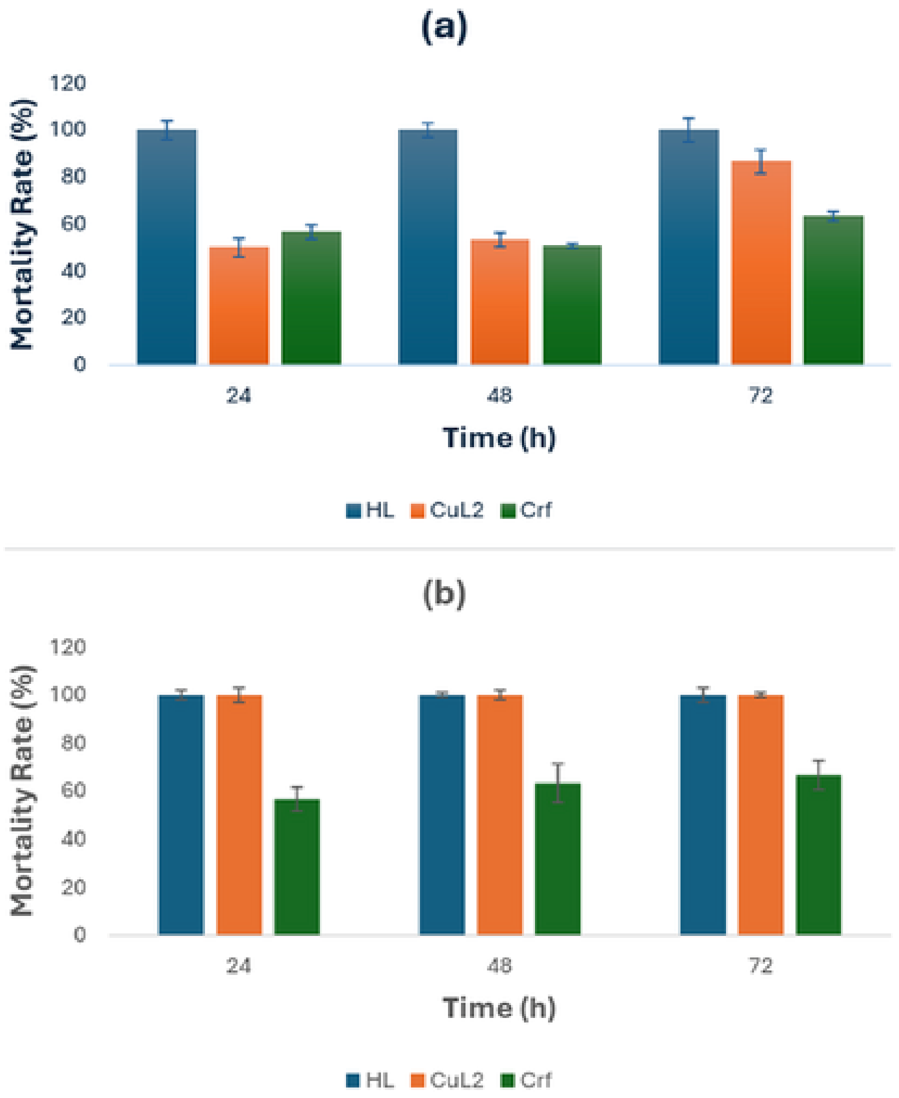

FIGURE 7. Plot of the mortality rate of the second stage juvenile (J2) after treatment with the ligand (HL), and its copper complex (CuL_2), comparative to control, carbofuran (Crf) as a function of time after 24, 48, and 72 h; using concentrations of (a) 50 µM and (b) 100 µM.

3.9.3 Egg-Hatching Inhibition Study

The egg hatching inhibition results (Figure 6a,b) showed that at a concentration of 50 µM, **HL** inhibited egg hatching by 100% at 24, 48, and 72 h, preventing any eggs from hatching. In comparison, treatment with **CuL_2** resulted in egg hatching inhibition rates of 93.86 ± 0.22%, 98.76 ± 0.14%, and 99.33%, after 24, 48, and 72 h of treatment, respectively (Figure 6a). In contrast, the control **Crf** inhibited egg hatching at rates of 56.33 ± 0.33%, 63.94 ± 0.61%, and 67.00 ± 0.34% after 24, 48, and 72 h of treatment, respectively (Figure 6a).

At a concentration of 100 µM, both **HL** and **CuL_2** achieved a 100% egg hatching inhibition at 24, 48, and 72 h of treatment (Figure 6b). In comparison, **Crf** achieved egg-hatching inhibition rates of 88.16 ± 0.84%, 89.90 ± 0.33%, and 90.80 ± 0.50% after 24, 48, and 72 h of treatment, respectively (Figure 6b). The higher egg hatching inhibition activity of the free ligand at lower concentrations is likely due to its better solubility and specific mode of action, while the complex's altered structure may initially hinder its efficacy. However, at higher concentrations, the modified structure of the complex becomes advantageous. Both the ligand and the complex outperform **Crf** at all concentrations, possibly due to synergistic effects, enhanced release of active species, and multiple targeting mechanisms, demonstrating their superior nematocidal activity

3.9.4 Mortality Rate Study

The efficacy of the complex (**CuL$_2$**) and the ligand (**HL**), compared to the control **Crf**, in influencing the mortality rate of second-stage juvenile (J2) nematodes was assessed by measuring the percentage of nematodes that perished after exposure to the compounds at concentrations of 50 and 100 µM over a 24–72-h treatment period. The results, depicted in (Figure 7a,b), show a trend like that observed in the egg hatching inhibition study. Specifically, when J2 were exposed to the compounds at a concentration of 50 µM, **HL** exhibited a mortality rate of 100% at 24, 48, and 72 h, respectively (Figure 7a). In comparison, exposure to **CuL$_2$** at the same concentration resulted in mortality rates of 56.66 ± 0.33%, 63.33 ± 0.23%, and 86.66 ± 0.13% at 24, 48, and 72 h, respectively (Figure 7b). The control, **Crf**, showed mortality rates of 50.00 ± 0.00%, 54.54 ± 0.64%, and 67.35 ± 0.54% at 24, 48, and 72 h, respectively. Similarly, at a higher concentration of 100 µM, exposure of J2 to **HL** and **CuL$_2$** led to a mortality rate of 100% after 24, 48, and 72 h of treatment, respectively (Figure 7b). Conversely, the control, **Crf**, exhibited mortality rates of 62.45 ± 0.64%, 68.66 ± 0.82%, and 78.45 ± 0.61% after 24, 48, and 72 h of treatment, respectively (Figure 7b).

The ligand demonstrating higher mortality rates than the complex at lower concentrations on the J2 nematodes could be attributed to factors such as its potentially greater solubility and specific mode of action, which may interact more effectively with the nematodes. Additionally, the ligand and the complex showing higher activity than carbofuran at all concentrations might stem from synergistic effects between the compounds, enhanced release of active species, multiple targeting mechanisms, and specific interactions with the nematodes, collectively contributing to their superior efficacy in inducing nematode mortality across the concentration range studied.

3.9.5 Mechanism of Action of HL and CuL$_2$

The antinematicidal activity of the synthesized compounds can be attributed to the presence of specific substituents as well as the role of the copper ion in the complex. The azomethine group in the **HL** interacts with vital biomolecules in the nematode, potentially disrupting key biochemical pathways. The trifluoromethoxy substituent enhances the compound's binding to biological targets and facilitates membrane penetration due to its lipophilic nature, impacting membrane integrity and cellular functions. The bromo substituent contributes to the compound's reactivity and affects its binding affinity to biological receptors or enzymes. In the copper complex, the copper ion's redox properties induce oxidative stress within the nematode, disrupting cellular redox processes crucial for its survival. Furthermore, the Lewis acidity of copper interferes with enzymatic functions, thereby enhancing the compounds' efficacy by affecting essential biological processes in the nematode. Collectively, the interactions of these substituents, including azomethine, trifluoromethoxy, and bromo groups, along with the properties of the copper ion in the complex, synergistically disrupt cellular processes, impact membrane integrity, and impede the nematode's growth and survival, culminating in the observed antinematicidal effects.

3.10 Computational Study

3.10.1 Analysis of the Optimized Geometries of HL and CuL_2

The optimized molecular structures of **HL** and **CuL_2** are displayed in Figure 8 with their respective frontier molecular orbital isosurfaces and ESP maps. The optimized geometries clearly reveal the occurrence of coordination between two molecules of the ligand (the deprotonated form) and Cu(II) ion, forming a stable and nearly perfect square planar shape, in agreement with the experimental proposition. Selected geometrical parameters (bond lengths and bond angles) confirming the square planar geometry of the complex are presented in Table 1 with the computed reactivity and thermodynamic descriptors.

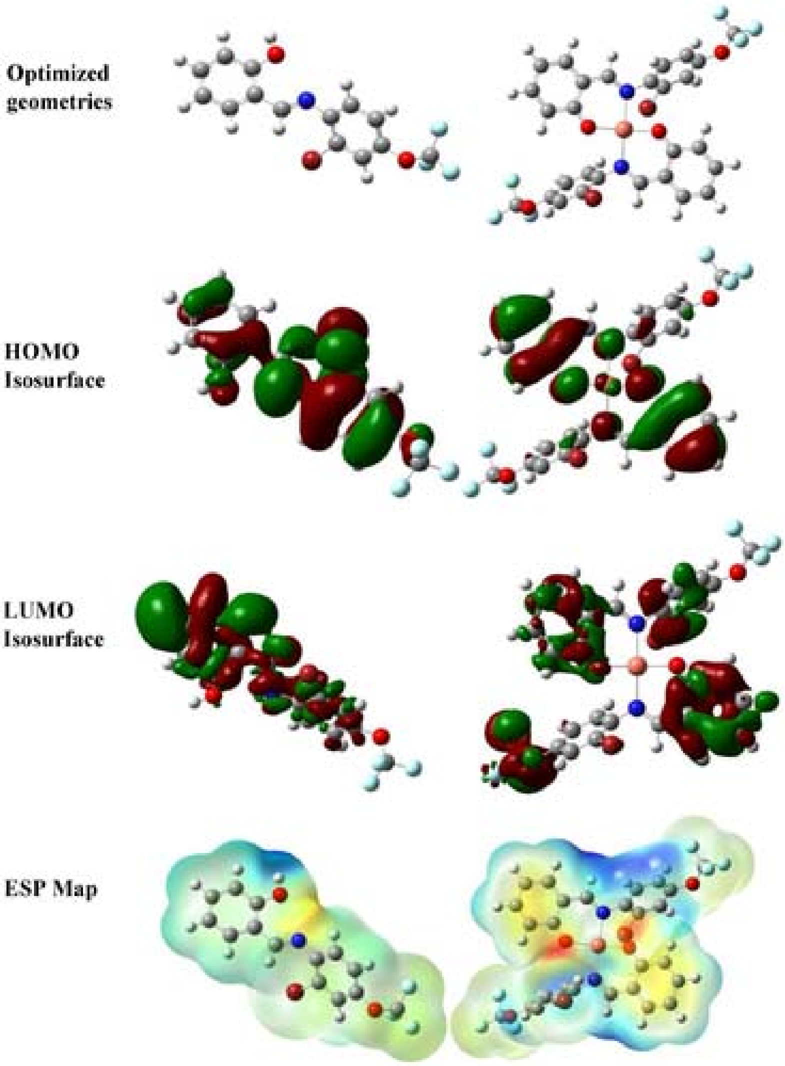

FIGURE 8. Optimized geometries of HL (left) and CuL_2 (right) showing their frontier molecular orbital isosurfaces and electrostatic potential maps.

TABLE 1. Predicted geometrical, reactivity, and thermodynamic descriptors for the compounds.

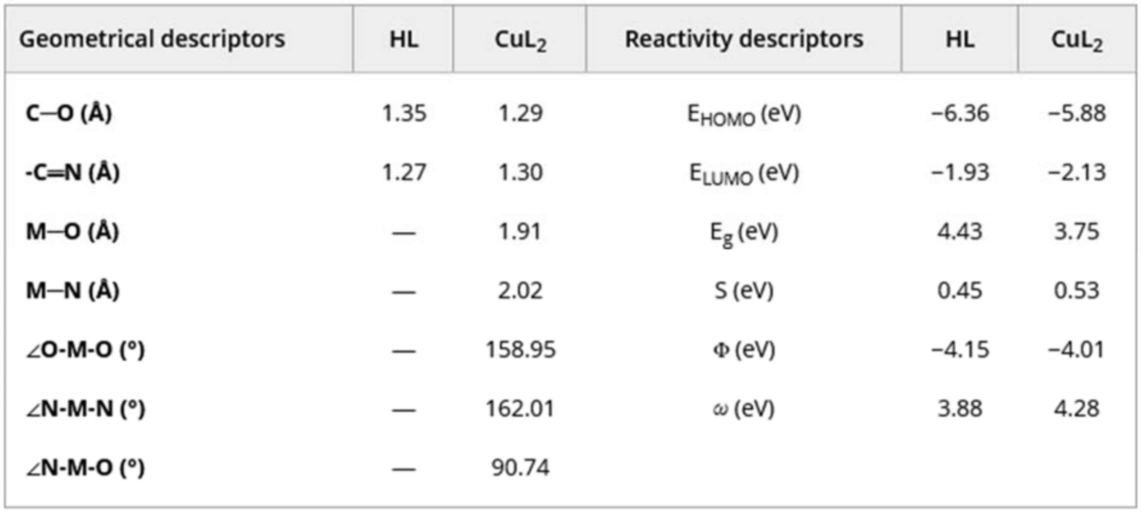

Geometrical descriptors	**HL**	**CuL$_2$**	**Reactivity descriptors**	**HL**	**CuL$_2$**
C─O (Å)	1.35	1.29	E_{HOMO} (eV)	−6.36	−5.88
-C═N (Å)	1.27	1.30	E_{LUMO} (eV)	−1.93	−2.13
M─O (Å)	—	1.91	E_g (eV)	4.43	3.75
M─N (Å)	—	2.02	S (eV)	0.45	0.53
∠O-M-O (°)	—	158.95	Φ (eV)	−4.15	−4.01
∠N-M-N (°)	—	162.01	ω (eV)	3.88	4.28
∠N-M-O (°)	—	90.74			

The variations in the lengths of C─O and C═N bonds between the ligand and the complex are indicative of a change in electron densities in these bonds upon their involvement in coordination with the metal ion. The lengths of the metal-ligand bonds (i.e., Cu─O and Cu─N) are within the required range [60], while the three bond angles (O-Cu-O, N-Cu-N, and N-Cu-O) are characteristic of a square planar configuration; the values of O-M-O and N-M-N indicate that the complex is almost planar whereas that of N-M-O is typical of the angle between two perpendicular bonds in a square planar geometry [61, 78].

3.11 Reactivity Analysis

The HOMO isosurface (Figure 8) marks the parts of the ligand and the complex that could be responsible for donating electrons to an electron-deficient species to foster a strong donor-acceptor interaction which is crucial in biological systems. On the other hand, the LUMO isosurface reveals the structural portions of the compounds having the highest electron deficiency. These portions are responsible for the electrophilic behavior of the compounds, that is, their propensity to nucleophilic attack. As evident from Figure 8, the HOMO isosurface spreads essentially over the entire delocalized *pi*-electron networks of both the ligand and the complex, encapsulating the donor moieties (C═O and C═N), and excluding the $-CF_3$ substituent in the case of the ligand as well as the rings bearing this substituent in the case of the complex. This obviously affirms the strong electron-withdrawing nature of $-CF_3$.

On the other hand, the LUMO isosurface covers the entire structures of the ligand and the complex with the exception of the hetero-atoms (O and N) and the substituents (-Br and $-OCF_3$). It is interesting to note the manner in which the LUMO isosurface is distributed between the two opposite rings bearing the $-OCF_3$ substituent in the complex. The effect of this substituent on both ends of the complex appears to be well controlled such that the electron density around the coordination region is not severely depleted to preserve the structural and electronic integrities of the complex. This suggests that the central metal atom played a crucial role in mediating an equitable electron density distribution between the opposite ends of the complex. On one end, the electron-withdrawing effect of $-OCF_3$ led to the depletion of electron density in the associated ring as revealed by the LUMO isosurface. To balance the electron density on both ends and preserve the electronic density at the coordination region, the opposite ring inductively pulled electrons from its -OCF_3, making it an electron-deficient moiety as confirmed by the appearance of LUMO isosurface on the second -OCF_3. We believe that this phenomenon would have a strong nexus with the biological activity of the complex.

Quantitatively, HOMO and LUMO energies are a pointer to electron-donating and electron-accepting tendencies, respectively. The higher the HOMO energy, the higher the tendency to donate electrons, and the lower the LUMO energy, the higher the probability to accept electrons. Therefore, the E_{HOMO} and E_{LUMO} values (Table 1) suggest that the complex is more likely to donate and accept electrons better than the ligand.

HOMO-LUMO energy gap (E_g) and softness () are parameters that describe the overall stability and propensity of a molecule to a change in electronic structure. The smaller the value of ΔE and the higher the size of , the more the ease of excitation, the smaller the reluctance to electronic perturbation, and the higher the activity of a molecule. Inferring from the results shown in Table 2, the complex is predicted to be more active than the ligand, in agreement with the trend of the biological study discussed previously. The mechanism of activity of the complex will be controlled both by its electron-donating and electron-accepting capabilities as revealed by its E_{HOMO} and E_{LUMO} values.

TABLE 2. Stabilization energies of the complex as obtained from natural bond orbital (NBO) calculation.

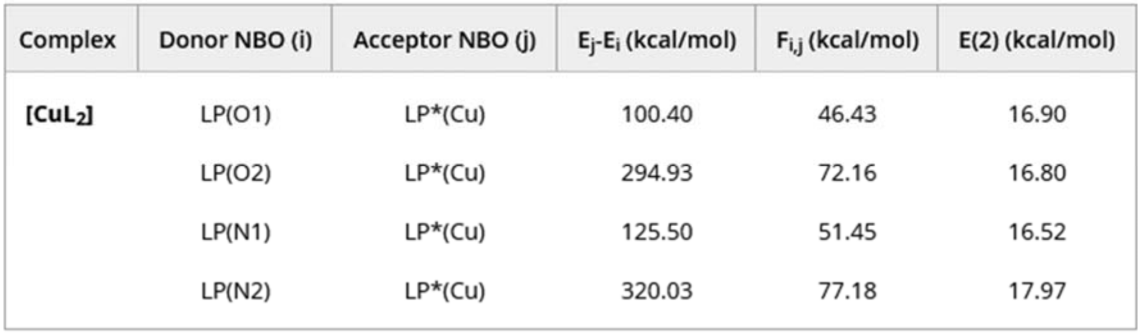

Complex	Donor NBO (i)	Acceptor NBO (j)	E_j-E_i (kcal/mol)	$F_{i,j}$ (kcal/mol)	E(2) (kcal/mol)
[CuL_2]	LP(O1)	LP*(Cu)	100.40	46.43	16.90
	LP(O2)	LP*(Cu)	294.93	72.16	16.80
	LP(N1)	LP*(Cu)	125.50	51.45	16.52
	LP(N2)	LP*(Cu)	320.03	77.18	17.97

The trend of chemical potential () corroborates the E_{HOMO}, suggesting that the complex possesses a higher electron-donating capacity. The electrophilicity index () reveals that the complex is more electrophilic than the ligand, implying that the complex will be more susceptible to the attack of a bio-nucleophile than the ligand.

The molecular ESP maps displayed in Figure 8 show the electron-rich and electron-deficient regions, thus, helping to identify the prospective sites for electrophilic and nucleophilic attacks in the compounds. The most electron-rich molecular region is shown in red whereas the most electron-deficient one is indicated with a blue color [41]. Regions marked by orange and yellow colors are moderately and weakly populated by electrons while the pale green regions are neither electron-deficient nor electron-rich, hence called regions of zero potential.

Using the color codes described above, the ESP map of the ligand (Figure 8) shows the presence of a substantial amount of electron density around the azomethine (HC═N) and carbonyl (C═O) functions, justifying the choice of these sites for coordination with the metal ion. As for the complex, the electron-deficient regions (areas colored blue) are a result of the electron-withdrawing influence of -OCF_3, further justifying the absence of HOMO isosurface in these areas. The phenyl rings indicated in yellow could be utilized for interaction with weak bio-electrophiles, hydrophobic interaction in biological systems, or *pi-pi* stacking which is crucial for obtaining the crystal of the complex.

3.12 Natural Bond Orbital Analysis of Metal-Ligand Bond Strength

The stabilization energy, E(2) helps to quantify the stability of the bonds formed between the metal ion and the ligand. This parameter is derived using the relation:

$$E(2) = q_j \frac{F(i,j)^2}{\epsilon_j - \epsilon_i} \tag{5}$$

where is the NBO Fock off-diagonal element, is the occupancy of the donor orbital, and and are energies of the donor and acceptor NBO, respectively, and are the diagonal elements of the matrix [57].

The E(2) values for the ligand's interaction with the metal ion through the donor sites of the ligand are presented in Table 2. The larger the E(2) value, the stronger the interaction and the more the stability of the metal-ligand bond which results from charge transfer from the ligand (donor) to the metal ion (acceptor). Thus, the E(2) values in the table indicate that the metal-ligand interaction through the two donor sites of the ligand (i.e., O and N) are strong and sufficiently stable. However, the interaction via the nitrogen site seems to be more favorable on average.

4 Conclusion

Herein, the fluoro-substituted **HL** and its copper(II) complex (**CuL_2**) were successfully synthesized and characterized. The solid-state structure of the complex was elucidated through X-ray single crystal diffraction analysis, confirming the formation of (**CuL_2**). Hirshfeld surface analyses of **CuL_2** highlighted the significant role of H···H interactions in stabilizing the self-assembly process, while the stability of **CuL_2** was further confirmed through time-dependent UV-vis spectroscopy. The nematicidal activities of **HL** and **CuL_2** were assessed through in vitro egg hatching inhibition and mortality rate assays, in comparison to the control, **Crf**. The results indicated that **HL** exhibited superior activity compared to **CuL_2** at a concentration of 50 µM, achieving both 100% egg-hatching inhibition and mortality rates over the 24–72-h testing period. Furthermore, at a concentration of 100 µM, both **HL** and **CuL_2** demonstrated complete efficacy in both assays. Moreover, both compounds surpassed the control (**Crf**) in terms of activity in both assays and at both concentrations over the 24–72-h testing period. These findings hold significant promise for the agricultural sector, opens up avenues for environmentally friendly and efficacious solutions in pest control, contributing to the advancement of agricultural practices towards more sustainable and effective pest management strategies.

Author Contributions

This study was a collaborative effort among all the authors, who contributed to its conception and design. The data acquisition, analysis, and interpretation were carried out collectively. The manuscript was meticulously drafted and underwent thorough revisions by all the authors to incorporate significant intellectual content. Final approval for the publication of the manuscript was granted by all authors, indicating their unanimous agreement and endorsement of the work.

Acknowledgments

Salisu Y. Lawan expresses gratitude to the Department of Soil Science, Faculty of Agriculture, University of Maiduguri, for their assistance with the nematicidal activity study. Waziri are grateful to the University of Johannesburg URC for the award of PDRF.

Conflicts of Interest

The authors declare no conflicts of interest.

Data Availability Statement

Deposition Number(s) 2393137 (for CuL_2) contain(s) the supplementary crystallographic data for this paper. These data are provided free of charge by the joint Cambridge Crystallographic Data Centre and

References

1. A. Afzal and T. Mukhtar, "Revolutionizing Nematode Management to Achieve Global Food Security Goals—An Overview," *Heliyon* 10 (2024): e25325.
2. D. L. Coyne, L. Cortada, J. J. Dalzell, et al., "Plant-Parasitic Nematodes and Food Security in Sub-Saharan Africa," *Annual Review of Phytopathology* 56 (2018): 381–403.
3. C. Kantor, J. D. Eisenback, and M. Kantor, "Biosecurity Risks to Human Food Supply Associated With Plant-Parasitic Nematodes," *Frontiers in Plant Science* 15 (2024): 1404335.
4. J. Desaeger, C. Wram, and I. Zasada, "New Reduced-Risk Agricultural Nematicides - Rationale and Review," *Journal of Nematology* 52 (2020): 1–16.
5. M. M. M. Abd-Elgawad, "Upgrading Strategies for Managing Nematode Pests on Profitable Crops," *Plants* 13 (2024): 1558.
6. T. C. Sparks, N. Storer, A. Porter, R. Slater, and R. Nauen, "Insecticide Resistance Management and Industry: The Origins and Evolution of the Insecticide Resistance Action Committee (IRAC) and the Mode of Action Classification Scheme," *Pest Management Science* 77 (2021): 2609–2619.
7. D. Pires, C. S. Vicente, E. Menéndez, et al., "The Fight Against Plant-Parasitic Nematodes: Current Status of Bacterial and Fungal Biocontrol Agents," *Pathogens* 11 (2022): 1178.
8. R. K. Jones, " Nematode Control and Nematicides: Developments Since 1982 and Future Trends," in: Nematology in South Africa: A View From the 21st Century, eds. H. Fourie, V. W. Spaull, R. K. Jones, M. S. Daneel, and D. De Waele (Cham: Springer, 2017): 129–150.
9. R. Baidoo, T. Mengistu, R. McSorley, R. H. Stamps, J. Brito, and W. T. Crow, "Management of Root-knot Nematode (Meloidogyne incognita) on Pittosporum tobira Under Greenhouse, Field, and On-farm Conditions in Florida," *Journal of Nematology* 49 (2017): 133.
10. M. R. Khan, Novel Biological and Biotechnological Applications in Plant Nematode Management (Singapore: Springer, 2023).
11. N. Sivasubramaniam, G. Hariharan, and M. C. M. Zakeel, " Sustainable Management of Plant-Parasitic Nematodes: An Overview From Conventional Practices to Modern Techniques," in: Management of Phytonematodes: Recent Advances and Future

Challenges, eds. R. A. Ansari, R. Rizvi, and I. Mahmood (Singapore: Springer, 2020): 353–399.

12. M. M. M. Abd-Elgawad, “Understanding Molecular Plant-Nematode Interactions to Develop Alternative Approaches for Nematode Control,” *Plants* 11 (2022): 2141.
13. M. M. M. Abd-Elgawad, “Optimizing Safe Approaches to Manage Plant-Parasitic Nematode,” *Plants* 10 (2021): 1911.
14. M. M. M. Abd-Elgawad, “Exploiting Plant-Phytonematode Interactions to Upgrades Safe and Effective Nematode Control,” *Life* 12 (2022): 1916.
15. M. M. M. Abd-Elgawad, “ Plant-Parasitic Nematodes and Their Biocontrol Agents: Current Status and Future Vistas,” in: Management of Phytonematodes: Recent Advances and Future Challenges, eds. R. A. Ansari, R. Rizvi, and I. Mahmood (Singapore: Springer, 2020): 171–203.
16. K. Roush, “Global Hunger,” *AJN the American Journal of Nursing* 123 (2023): 17.
17. J. Gyimah, B. M. Saalidong, and L. K. Nibonmua, “The Battle to Achieve Sustainable Development Goal Two: The Role of Environmental Sustainability and Government Institutions,” *PLoS ONE* 18 (2023): e0291310.
18. E. J. Medina-Hernández, D. S. Guzmán-Aguilar, J. L. Muñiz-Olite, and L. R. Siado-Castañeda, “The Current Status of the Sustainable Development Goals in the World,” *Development Studies Research* 10 (2023): 2163677.
19. K. Shulla and W. Leal-Filho, “Achieving the UN Agenda 2030: Overall Action for the Successful Implementation of the Sustainable Development Goals Before and After the 2030 Deadline,” European Union Parliament's Online Database (2023): 1–64.
20. S. Mushtaq, H. Tak, J. H. Sheikh, and I. M. MalikU.-un-Nisa, “Plant Parasitic Nematode Management Using Antagonistic Plants as a Potential Substitute to Hazardous Chemical Control—A Review,” *International Journal of Pest Management* (2024), https://doi.org/10.1080/09670874.2024.2399069.
21. F. Forghani and A. Hajihassani, “Recent Advances in the Development of Environmentally Benign Treatments to Control Root-Knot Nematodes,” *Frontiers in Plant Science* 11 (2020): 1125.
22. S. Kumar, A. Arora, V. K. Maikhuri, et al., “Advances in Chromone-based Copper(ii) Schiff Base Complexes: Synthesis, Characterization, and Versatile Applications in Pharmacology and Biomimetic Catalysis,” *RSC Advances* 14 (2024): 17102.
23. I. Tsacheva, Z. Todorova, D. Momekova, G. Momekov, and N. Koseva, “Pharmacological Activities of Schiff Bases and Their Derivatives With Low and High Molecular Phosphonates,” *Pharmaceuticals* 16 (2023): 938.
24. S. Dudhat and S. Kulkarni, *International Journal of Engineering Technology Science and Research* 5 (2018): 740.
25. R. Golbedaghi, A. M. Tabanez, S. Esmaeili, and R. Fausto, “Biological Applications of Macrocyclic Schiff Base Ligands and Their Metal Complexes: A Survey of the Literature (2005–2019),” *Applied Organometallic Chemistry* 34 (2020): e5884.
26. A. Subhash J. Chaudhary, M. Kumar, N. Kumar, and N. K. Agarwal, “Synthesis, Spectroscopic Characterization, Biocidal Evaluation Molecular Docking & DFT Investigation of 16-18 Membered Macrocyclic Complexes of Cobalt (II),” *Journal of Chemical Sciences* 134 (2022): 113.
27. P. Gull and A. A. Hashmi, “Biological Activity Studies on Metal Complexes of Macrocyclic Schiff Base Ligand: Synthesis and Characterization,” *Journal of the Brazilian Chemical Society* 26 (2015): 1331.
28. L. Ekta, “Metal Complexes Derived From Schiff Base Ligand System as Potential Nematicidal Agents,” *Journal of Chemical and Pharmaceutical Resources* 4 (2013): 11–28.

29. M. S. El-Attar, N. S. Abd El-Lattif, and S. A. Sadeek, “Study on the Nematicidal Activity and Chemical Structure of NO Bidentate Schiff Base Some Metal Complexes,” *Journal of the Chinese Chemical Society* 67 (2020): 610.
30. R. Meena and N. Fahmi, “Nematicidal Activity of Vanadium(V) Complexes Derived From Schiff Base Against *Meloidogyne Incognita*,” *Journal of Biotechnology Bioengineering and Research* 4 (2013): 437.
31. P. Kavitha and K. L. Reddy, “Synthesis, Structural Characterization, and Biological Activity Studies of Ni(II) and Zn(II) Complexes,” *Bioinorganic Chemistry and Applications* 2014 (2014): 1.
32. P. Kavitha, M. R. Chary, B. Singavarapu, and K. L. Reddy, “Synthesis, Characterization, Biological Activity and DNA Cleavage Studies of Tridentate Schiff Bases and Their Co(II) Complexes,” *Journal of Saudi Chemical Society* 20 (2016): 69.
33. B. Das, A. T. Baidya, S. Chakrabarti, et al., “Synthesis and Biological Evaluation of Halogen-Substituted Novel α-Ketoamides as Potential Protein Aggregation Modulators in Alzheimer's Disease,” *Bioorganic Chemistry* 147 (2024): 107373.
34. I. Waziri, M. T. Kelani, M. O. Oyedeji-Amusa, et al., “Synthesis and Computational Investigation of N,N-Dimethyl-4-[(Z)-(phenylimino)methyl]aniline Derivatives: Biological and Quantitative Structural Activity Relationship Studies,” *Journal of Molecular Structure* 1276 (2023): 134756.
35. I. Waziri, T. L. Yusuf, E. Akintemi, M. T. Kelani, and A. Muller, “Spectroscopic, Crystal Structure, Antimicrobial and Antioxidant Evaluations of New Schiff Base Compounds: An Experimental and Theoretical Study,” *Journal of Molecular Structure* 1273 (2023): 134382.
36. M. Z. Hernandes, S. M. T. Cavalcanti, D. R. M. Moreira, W. F. de Azevedo Junior, and A. C. L. Leite, “Halogen Atoms in the Modern Medicinal Chemistry: Hints for the Drug Design,” *Current Drug Targets* 11 (2010): 303.
37. T. L. Yusuf, I. Waziri, K. A. Olofinsan, E. O. Akintemi, E. C. Hosten, and A. J. Muller, “Evaluating the In Vitro Antidiabetic, Antibacterial and Antioxidant Properties of Copper(II) Schiff Base Complexes: An Experimental and Computational Studies,” *Journal of Molecular Liquids* 389 (2023): 122845.
38. N. Kordestani, H. A. Rudbari, A. R. Fernandes, et al., “Copper(II) Complexes With Tridentate Halogen-Substituted Schiff Base Ligands: Synthesis, Crystal Structures and Investigating the Effect of Halogenation, Leaving Groups and Ligand Flexibility on Antiproliferative Activities,” *Dalton Transactions* 50 (2021): 3990.
39. I. Waziri, T. L. Yusuf, H. A. Zarma, S. O. Oselusi, L.-C. C. Coetzee, and A. S. Adeyinka, “New Palladium (II) Complexes From Halogen Substituted Schiff Base Ligands: Synthesis, Spectroscopic, Biological Activity, Density Functional Theory, and Molecular Docking Investigations,” *Inorganica Chimica Acta* 552 (2023): 121505.
40. R. M. Elsamra, M. S. Masoud, and A. M. Ramadan, “Designing Metal Chelates of Halogenated Sulfonamide Schiff Bases as Potent Nonplatinum Anticancer Drugs Using Spectroscopic, Molecular Docking and Biological Studies,” *Scientific Reports* 12 (2022): 20192.
41. S. Y. Lawan, M. B. Mshelia, G. A. Mala, et al., “Antioxidant Activity and DFT Calculations of Metal Complexes Derived From a Schiff Base Ligand: Synthesis, Characterization, and Biological Evaluation,” *ChemistrySelect* 9 (2024): e202400676.
42. I. Waziri, M. T. Kelani, M. O. Oyedeji-Amusa, A. K. Oyebamiji, L.-C. C. Coetzee, and A. J. Muller, “Comparative Investigation of Derivatives of (E)-N-((E)-3-phenylallylidene)aniline: Synthesis, Structural Characterization, Biological Evaluation, Density Functional Theory Analysis, and In Silico Molecular Docking,” *Heliyon* 10 (2024): e26632.

43. I. Waziri, H. M. Masena, T. L. Yusuf, L.-C. C. Coetzee, A. S. Adeyinka, and A. J. Muller, "Synthesis, Characterization, Biological Evaluation, DFT and Molecular Docking Studies of (Z)-2-((2-bromo-4-chlorophenyl)imino)methyl-4-chlorophenol and Its Co(II), Ni(II), Cu(II), and Zn(II) Complexes," *New Journal of Chemistry* 47 (2023): 17853.
44. A. Bruker and B. SAINT, "Phase Annealing in SHELX-90: Direct Method for Larger Structures," *Acta Crystallography Section A: Foundation of Crystallography* 46 (1990): 467.
45. T. Schulz, K. Meindl, D. Leusser, et al., "A Comparison of a Microfocus X-ray Source and a Conventional Sealed Tube for Crystal Structure Determination," *Journal of Applied Crystallography* 42 (2009): 885.
46. G. M. Sheldrick, "Crystal Structure Refinement with SHELXL," *Acta Crystallographica Section C: Structural Chemistry* 71 (2015): 3.
47. C. F. Macrae, I. Sovago, S. J. Cottrell, et al., "Mercury 4.0: From Visualization to Analysis, Design and Prediction," *Journal of Applied Crystallography* 53 (2020): 226.
48. C. F. Macrae, I. J. Bruno, J. A. Chisholm, et al., "Mercury CSD 2.0 – New Features for the Visualization and Investigation of Crystal Structures," *Journal of Applied Crystallography* 41 (2008): 466.
49. C. B. Pinto, B. L. Rodrigues, and L. H. Dos Santos, "Estimating Electron Density at the Bond Critical Point Through Atomic Hirshfeld Surfaces," *Journal of Applied Crystallography* 54 (2021): 1600–1605.
50. R. Heydari, E. Pourjam, and E. M. Goltapeh, "Antagonistic Effect of Some Species of Pleurotus on the Root-Knot Nematode, Meloidogyne javanica In Vitro," *Plant Pathology Journal* 5 (2006): 173.
51. L. A. Curtiss, K. Raghavachari, P. C. Redfern, V. Rassolov, and J. A. Pople, "Gaussian-3 (G3) Theory for Molecules Containing First and Second-Row Atoms," *Journal of Chemical Physics* 109 (1998): 7764.
52. L.-C. C. Coetzee, A. S. Adeyinka, and N. Magwa, "A Theoretical Investigation of Decorated Novel Triazoles as DSSCs in PV Devices," *Journal of Molecular Modeling* 27 (2021): 353.
53. A. D. Becke, "Density-Functional Thermochemistry. I. The Effect of the Exchange-Only Gradient Correction," *Journal of Chemical Physics* 96 (1992): 2155.
54. C. Lee, W. Yang, and R. G. Parr, "Development of the Colle-Salvetti Correlation-Energy Formula Into a Functional of the Electron Density," *Physical Review B* 37 (1988): 785.
55. F. Weigend and R. Ahlrichs, "Balanced Basis Sets of Split Valence, Triple Zeta Valence and Quadruple Zeta Valence Quality for H to Rn: Design and Assessment of Accuracy," *Physical Chemistry Chemical Physics* 7 (2005): 3297.
56. T. Lu and F. Chen, "Atomic Dipole Moment Corrected Hirshfeld Population Method," *Journal of Theoretical and Computational Chemistry* 11 (2012): 163.
57. H. Kargar, M. Fallah-Mehrjardi, R. Behjatmanesh-Ardakani, et al., "Diverse Coordination of Isoniazid Hydrazone Schiff Base Ligand Towards Iron(III): Synthesis, Characterization, SC-XRD, HSA, QTAIM, MEP, NCI, NBO and DFT Study," *Journal of Molecular Structure* 1250 (2022): 131691.
58. H. Kargar, P. Forootan, M. Fallah-Mehrjardi, et al., "Novel Oxovanadium and Dioxomolybdenum Complexes of Tridentate ONO-Donor Schiff Base Ligand: Synthesis, Characterization, Crystal Structures, Hirshfeld Surface Analysis, DFT Computational Studies and Catalytic Activity for the Selective Oxidation of Benzylic Alcohols," *Inorganica Chimica Acta* 523 (2021): 120414.

59. H. Kargar, M. Ashfaq, M. Fallah-Mehrjardi, R. Behjatmanesh-Ardakani, K. S. Munawar, and M. N. Tahir, "Synthesis, Crystal Structure, Spectral Characterization, Theoretical and Computational Studies of Ni(II), Cu(II) and Zn(II) Complexes Incorporating Schiff Base Ligand Derived From 4-(diethylamino)salicylaldehyde," *Inorganica Chimica Acta* 536 (2022): 120878.
60. O. O. Wahab, L. O. Olasunkanmi, K. K. Govender, and P. P. Govender, "Synergistic Effect of Opposite Polar Substituents on Selected Properties of Disperse Yellow 119 dye," *Chemical Physics Letters* 704 (2018): 55.
61. O. O. Wahab, L. O. Olasunkanmi, K. K. Govender, and P. P. Govender, "Tuning the Aqueous Solubility, Chemical Reactivity and Absorption Wavelength of Azo Dye Through Systematic Adjustment of Molecular Charge Density: A DFT Study," *Molecular Physics* 118 (2020): e1626508.
62. I. Waziri, O. O. Wahab, G. Mala, S. Oselusi, S. Egieyeh, and H. Nasir, "Zinc(II) Complex of (Z)-4-((4-nitrophenyl)amino)pent-3-en-2-one, a Potential Antimicrobial Agent: Synthesis, Characterization, Antimicrobial Screening, DFT Calculation and Docking Study," *Bulletin of the Chemical Society of Ethiopia* 37 (2023): 633.
63. O. O. Wahab, L. O. Olasunkanmi, K. K. Govender, and P. P. Govender, "DMol3/COSMO-RS Prediction of Aqueous Solubility and Reactivity of Selected Azo Dyes: Effect of Global Orbital Cut-Off and COSMO Segment Variation," *Journal of Molecular Liquids* 249 (2018): 346.
64. T. L. Yusuf, D. C. Akintayo, S. D. Oladipo, et al., "The Effect of Structural Configuration on the DNA Binding and In Vitro Antioxidant Properties of New Copper(ii) N2O2 Schiff Base Complexes," *New Journal of Chemistry* 46 (2022): 12968.
65. T. L. Yusuf, S. D. Oladipo, S. Zamisa, et al., "Design of New Schiff-Base Copper(II) Complexes: Synthesis, Crystal Structures, DFT Study, and Binding Potency Toward Cytochrome P450 3A4," *ACS Omega* 6 (2021): 13704.
66. C. B. Pinto, B. L. Rodrigues, and L. H. Dos Santos, "Estimating Electron Density at the Bond Critical Point Through Atomic Hirshfeld Surfaces," *Journal of Applied Crystallography* 54 (2021): 1600.
67. M. A. Raza, D. Necmi, O. E. DOĞAN, A. Tuğgan, and S. H. Sumrra, "Synthesis of Two New Schiff Bases; Crystal Structure, Hirshfeld Surface Analysis, Density Functional Theory and Molecular Docking," *Journal of Molecular Structure* 1226 (2021): 129330.
68. C. Mchiri, L.-C. C. Coetzee, F. Chandoul, et al., "Synthesis, Characterization, DFT and Photocatalytic Studies of a New Pyrazine Cadmium(II) Tetrakis(4-methoxy-phenyl)-porphyrin Compound," *Molecules (Basel, Switzerland)* 27 (2022): 3833.
69. D. Majumdar, A. Frontera, R. M. Gomila, S. Das, and K. Bankura, "Synthesis, Spectroscopic Findings and Crystal Engineering of Pb(II)–Salen Coordination Polymers, and Supramolecular Architectures Engineered by σ-hole/spodium/tetrel Bonds: A Combined Experimental and Theoretical Investigation," *RSC Advances* 12 (2022): 6352.
70. M. J. Turner, S. Grabowsky, D. Jayatilaka, and M. A. Spackman, "Accurate and Efficient Model Energies for Exploring Intermolecular Interactions in Molecular Crystals," *Journal of Physical Chemistry Letters* 5 (2014): 4249.
71. J. Shelnutt and V. Ortiz, "Substituent Effects on the Electronic Structure of Metalloporphyrins: A Quantitative Analysis in Terms of Four-Orbital-Model Parameters," *Journal of Physical Chemistry* 89 (1985): 4733.

72. R. Tiwari and M. Nath, "Synthesis of 2-Nitro-3-(pyrrol-1-yl)-5,10,15,20-tetraarylporphyrins via a Clauson-Kaas Reaction and the Study of Their Electronic Properties," *New Journal of Chemistry* 39 (2015): 5500.
73. O. Khaoua, S. Mouffouk, N. Benbellat, et al., "Synthesis, Characterisation, Hirshfeld Surface Analysis, Magnetic Susceptibility, DFT Calculations, pkCSM Profile, and Biological Activities of Novel Mono-, Di-, and Multinuclear Cobalt (II) Complexes," *European Journal of Inorganic Chemistry* (2024): e202400033.
74. U. Mandal, C. Rizzoli, B. Chakraborty, D. Bandyopadhyay, and S. Mandal, "Synthesis, Crystal Structure, Hirshfeld Surface Analysis and Characterization of Two New Mononuclear Ni(II) Complexes," *Journal of Molecular Structure* 1302 (2024): 137420.
75. I. Ketata, L. Bejaoui, A. Brahmia, and R. B. Hassen, "Synthesis, Crystal Structure, Hirshfeld Surface Analysis, Spectroscopic Characterizations and Electrical Properties of the New Complex of Cobalt (III) and the Schiff-Base of Dihydroxycoumarin," *Journal of Molecular Structure* 1246 (2021): 131161.
76. D. van der Westhuizen, D. I. Bezuidenhout, and O. Q. Munro, "Cancer Molecular Biology and Strategies for the Design of Cytotoxic Gold(I) and Gold(III) Complexes: A Tutorial Review," *Dalton Transactions* 50 (2021): 17413.
77. E. Alessio, "Thirty Years of the Drug Candidate NAMI-A and the Myths in the Field of Ruthenium Anticancer Compounds: A Personal Perspective," *European Journal of Inorganic Chemistry* 2017 (2017): 1549.
78. K. Choroba, B. Machura, A. Szlapa-Kula, et al., "Square Planar Au(III), Pt(II) and Cu(II) Complexes With Quinoline-Substituted 2,2′:6′,2″-Terpyridine Ligands: From In Vitro to In Vivo Biological Properties," *European Journal of Medicinal Chemistry* 218 (2021): 113404.